Journal of Applied Geophysics 91 (2013) 66–81

Contents lists available at SciVerse ScienceDirect

Journal of Applied Geophysics

journal homepage: www.elsevier.com/locate/jappgeo

Locating near-surface scatterers using non-physical scattered waves resulting from seismic interferometry

U. Harmankaya [a], A. Kaslilar [a,*], J. Thorbecke [b], K. Wapenaar [b], D. Draganov [b]

[a] Department of Geophysical Engineering, Faculty of Mines, Istanbul Technical University, Istanbul, Turkey
[b] Sec. Applied Geophysics and Petrophysics, Dept. of Geoscience and Engineering, Delft University of Technology, The Netherlands

ARTICLE INFO

Article history:
Received 26 October 2012
Accepted 11 February 2013
Available online 18 February 2013

Keywords:
Locating scatterers and diffractors
Ghost scattered surface and body waves
Active source seismic interferometry
Inversion
Near-surface
Finite-difference modelling

ABSTRACT

We use controlled-source seismic interferometry (SI) and inversion in a unique way to estimate the location of near-surface scatterers and a corner diffractor by using non-physical (ghost) scattered surface and body waves. The ghosts are arrivals obtained by SI due to insufficient destructive interference in the summation process of correlated responses from a boundary of enclosing sources. Only one source at the surface is sufficient to obtain the ghost scattered wavefield. We obtain ghost scattered waves for several virtual-source locations. To determine the location of the scatterer, we invert the obtained ghost traveltimes by solving the inverse problem. We demonstrate the method using scattered surface waves. We perform finite-difference numerical simulations of a near-surface scatterer starting with a very simple model and increase the complexity by including lateral inhomogeneity. Especially for the model with lateral variations, we show the effectiveness of the method and demonstrate the estimation of the subsurface location of a corner diffractor using S-waves. In all models we obtain very good estimations of the location of the scatterer.

1. Introduction

The investigation and detection of near-surface structures such as cavities, caves, sinkholes, tunnels, mineshafts, buried objects, archeological ruins, water reservoirs and similar is important to mitigate geo- and environmental hazards (Culshaw and Waltham, 1987). These near-surface structures, (henceforth called scatterers) may pose risk during and after the construction of buildings, transportation ways (roads, highways, railways) or power plants (wind, solar, etc.), which are spread on wide areas. Furthermore, these scatterers can be affected by the changes in the hydraulic regime, earthquakes and change of the loading on the soil and thus may cause risk. Therefore, the detection, monitoring and stabilization of this type of weak zones is important to prevent environmental and geo hazards.

Especially, the detection of natural (karstic structures and caves) and man-made (tunnels, mine shafts and galleries) cavities is widely studied in the literature. Both numerical and/or field experiments are performed for this purpose. Several geophysical methods are available for investigation of the near-surface structures and each has advantages and disadvantages (McCann et al., 1987). The success depends on the resolution and penetration achieved by each method. Ground penetrating radar (GPR) (Al-fares et al., 2002; Nuzzo et al., 2007), microgravity and multi-channel analysis of surface waves (Debeglia et al., 2006; Samyn et al., 2012; Xu and Butt, 2006), seismic refraction and electric resistivity (Cardarelli et al., 2010; Nuzzo et al., 2007), seismic refraction only (Engelsfeld et al., 2008, 2011), are some examples for the exploited methods that are used for detecting the cavities. Some examples of geological studies on cavities and related geohazards are found in Culshaw and Waltham (1987), Woodcock et al. (2006), Edmonds (2008) and Khomenko (2008).

In seismic methods, a high-accuracy subsurface image of the shallow objects can be obtained using reflected body waves. This, though, requires high-resolution data acquired in a dense spatial array. These are not easily available for shallow-seismic applications. Furthermore, it might not always be possible to place active sources above the target scatterer or even close enough to it. In such cases, using sources away and having the generated wavefields propagate through unknown inhomogeneities might distort the results significantly. Surface waves are widely used in global, exploration and near-surface geophysics. A notable difference in the applications is the frequency content and the array aperture of the measurements that affect the investigation depth. The dispersive property of surface waves allows the estimation of the S-wave velocity structure and attenuation of shallow layers. In global seismology, surface waves are used to investigate the crust and upper-mantle structure (e.g. Chang and Baag, 2005; Cong and Mitchell, 1998; Kovach, 1978) and the source properties of seismic events (e.g. Canıtez and Toksöz, 1971; Ekström, 2006). In geotechnical engineering, S-wave velocity estimation from surface waves has become a popular tool and different active and passive-source techniques are applied (Bozdag and Kocaoglu, 2005; Foti, 2000; Kocaoglu and Fırtana, 2011; Leparoux et al., 2000; Nazarian et al., 1983; O'Neill, 2003; Park et al., 1999; Rix et al., 1998; Socco and Boiero, 2008; Socco et al., 2009, 2010) to obtain the near-surface

* Corresponding author. Tel.: +90 5334874389; fax: +90 2122856201.
E-mail addresses: kaslilar@itu.edu.tr, kaslilar@gmail.com (A. Kaslilar).

0926-9851/$ – see front matter © 2013 Elsevier B.V. All rights reserved.
http://dx.doi.org/10.1016/j.jappgeo.2013.02.004

properties of the medium. The surface-wave methods work under the assumption of laterally homogeneous stratified layers. Therefore lateral inhomogeneities, such as cavities or varying overburden thickness and steeply dipping bedrock cause difficulties in the estimation of the velocity structure and in the evaluation of the lateral inhomogeneities on the dispersion curve. However, Nasseri-Moghaddam et al. (2005), Bodet et al. (2010) and Boiero and Socco (2010) show the possibility of exploiting surface-wave dispersion curves to investigate voids and lateral variations of the subsurface.

Another methodology that is used for detecting the near-surface structures is that with scattered waves. Scattering of P-waves are used by Grandjean and Leparoux (2004), Gelis et al. (2005), Rodríguez-Castellanos et al. (2006), Mohanty (2011); coda waves are used by Mikesell et al. (2012); and scattered surface waves are used by Snieder (1987), Herman et al. (2000), Leparoux et al. (2000), Campman et al. (2004), Grandjean and Leparoux (2004), Gelis et al. (2005), Campman and Riyanti (2007), Kaslilar (2007), Xia et al. (2007), Chai et al. (2012). Based on seismic interferometry the scattered surface waves are studied in detail by Halliday and Curtis (2009).

We propose to use non-physical (ghost) scattered body and/or surface waves, obtained by seismic interferometry (SI), in an inversion scheme to estimate the location of a scatterer (Harmankaya et al., 2012a,b). The appearance of the ghost scattered waves is explained later in this section. SI traditionally refers to the method of retrieving the interreceiver wavefield by cross-correlating the wavefields recorded at each of the receivers (e.g. Snieder, 2004; van Manen et al., 2006; Wapenaar, 2004; Wapenaar and Fokkema, 2006). SI can be divided into controlled-source and passive methods. Controlled-source SI (Schuster et al., 2004) involves cross-correlation followed by summation over different controlled source positions at a boundary, while passive SI is the methodology of turning passive seismic measurements, like ambient noise and earthquakes, into impulsive seismic responses (Draganov et al., 2007, 2009; Roux et al., 2005; Ruigrok et al., 2010; Shapiro and Campillo, 2004). While SI has proven useful in retrieving surface-wave waveforms from passive noise sources (e.g. Halliday and Curtis, 2008; Sens-Schönfelder and Wegler, 2006; Snieder and Wapenaar, 2010), it is also shown that active-source signals can be used to synthesize interreceiver surface-wave estimates, which can be used, for example, for predictive ground-roll removal (Dong et al., 2006; Halliday et al., 2007, 2010).

To obtain the complete Green's function between the receivers whose recorded responses we cross-correlate, the boundary sources (primary or secondary) effectively need to enclose these receivers (Wapenaar and Fokkema, 2006). When the receivers are not equally illuminated from all directions by the boundary sources, ghost arrivals will appear in the SI result (Snieder et al., 2006). Furthermore, the physical arrivals might not be retrieved correctly. When using active sources at the surface, as is the standard practice for near-surface seismics, reflection ghosts will nearly always be present. The reflection ghosts are arrivals retrieved from the correlation of two reflected events in the active data, whose traveltimes correspond to reflections as if measured with sources and receivers redatumed in the subsurface at the levels of reflectors (Draganov et al., 2012; King and Curtis, 2012). This type of ghosts is called spurious reflections by Snieder et al. (2006). The limited number of the used sources might make the problem with the retrieved reflection ghosts even worse.

One way of addressing this problem is to try to retrieve only specific parts of the Green's function, for example only surface waves. For this, having sufficient boundary sources only in the stationary-phase regions for the retrieval of these specific parts would be enough (Snieder, 2004). For an inhomogeneous medium, the stationary-phase region for retrieval of direct surface waves between two receivers lies along the ray connecting the receivers and away from them. The boundary sources need to be present at the surface, but also down to a certain depth, depending on the specific medium characteristics. When only sources at the surface are used, the fundamental mode of the surface wave will be retrieved correctly, while the higher modes will be retrieved incorrectly (Kimman and Trampert, 2010). For retrieval of body-wave reflections between the two receivers at the surface, the stationary-phase region lies in the subsurface along the specular ray for that reflection arrival. The specular ray is the line in the subsurface, along which a wavefield will first be recorded at one of the receivers and after reflecting from the target subsurface reflector will be recorded at the second receiver. Using stationary-phase arguments, it can be shown that the subsurface boundary-source positions can be projected to surface positions along the specular-ray paths. This process, though, has as a consequence that reflection ghosts will be retrieved (Draganov et al., 2012; King and Curtis, 2012).

Retrieval of scattered surface waves follows the same logic as the retrieval of reflections, but the specular ray is along the surface. Halliday et al. (2010) show a field application of SI for retrieval of direct and off-line scattered surface waves by using a densely sampled 2D patch of active sources. Unfortunately, in near-surface seismics such dense source geometries are not common. Most likely, the active sources will be along a line or along several lines with a certain distance between them. This would mean that off-line scatterers would most likely result in the retrieval of ghost scattered surface waves. A subsurface scatterer will nearly always give rise to ghost scattered body waves.

In the following, we show that a limited number of available active surface sources is sufficient for locating a subsurface scatterer and estimating its location. We use modelled surface and body waves and show that even one active source is sufficient to obtain ghost scattered waves. In the next section, the calculation of the ghost scattered wavefield and the estimation procedure for the location of a point scatterer is given in detail using a dataset modelled according to an integral representation of the scattered wavefield. For inversion of the obtained ghost field, we use Singular Value Decomposition (SVD) and as a complementary method — the grid search method. The qualities of the estimations are provided by preparing the model resolution, data resolution and model covariance matrices. In Section 3, we test our method using finite-difference modelled data for models with increasing complexity — scatterer in a halfspace, scatterer and a corner diffractor in a medium with lateral velocity variation. As SI effectively redatums sources (or receivers) from places away from the scatterers to the target area (the location close to the structure of interest), the unwanted extra effects, due to propagation from sources through the laterally changing medium to the receivers close to the target area, are eliminated and the scatterer location can be estimated successfully. The discussions and conclusions are given in Sections 4 and 5, respectively.

2. Method

2.1. Ghost scattered waves obtained by SI

SI traditionally refers to the method of retrieving the interreceiver wavefield by cross-correlating the wavefields recorded at each of the receivers (e.g. Snieder, 2004; van Manen et al., 2006; Wapenaar, 2004; Wapenaar and Fokkema, 2006). In non-ideal situations apart from the true wavefield non-physical events will also occur. In this study, we use non-physical scattered body and surface waves in inversion to estimate the location of a scatterer. SI is applied to the scattered wavefield obtained from the seismic records of the original geometry by using only one source and by cross-correlating the reference trace d^{VS} (the trace at the virtual-source position) with the rest of the traces, d^i, which are present on the seismic record. This relation is

$$C_{d^i d^{VS}}(\tau) = \sum_n d^i(t_n)\, d^{VS}(t_n + \tau). \quad (1)$$

Note that the complete SI relation, as derived by Wapenaar and Fokkema (2006) requires a second summation over active sources

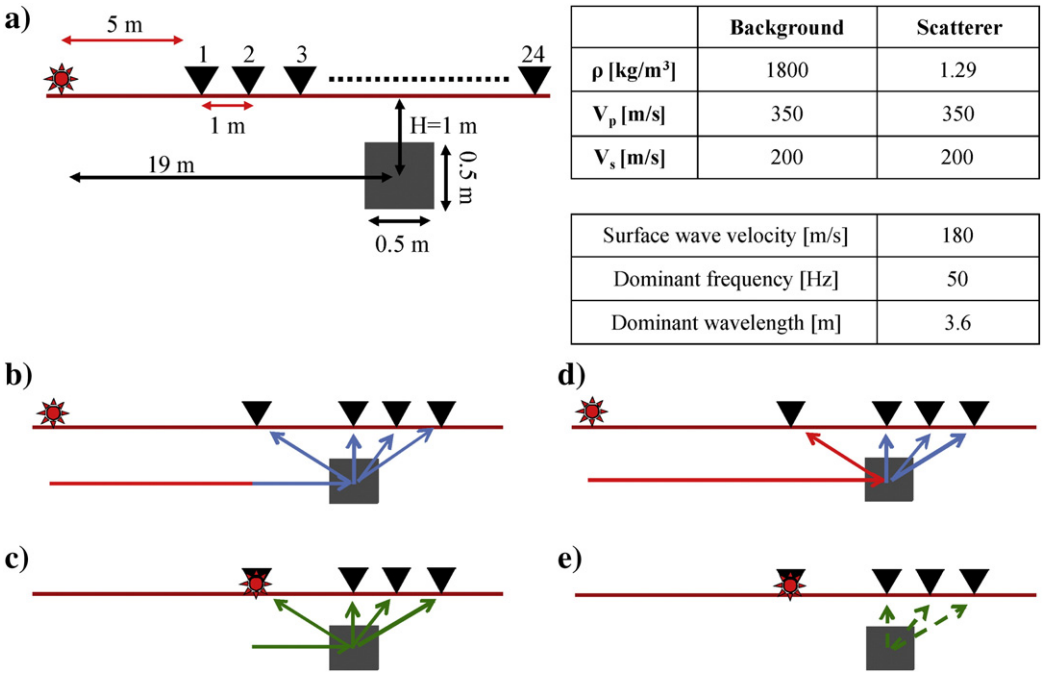

	Background	Scatterer
ρ [kg/m³]	1800	1.29
V_p [m/s]	350	350
V_s [m/s]	200	200

Surface wave velocity [m/s]	180
Dominant frequency [Hz]	50
Dominant wavelength [m]	3.6

Fig. 1. Schematic view of the model (left): the source (star), receivers (triangles) and scatterer (gray square). The modelling parameters for the background medium and the scatterer are given in the table (right). (b) Schematic ray paths for the active-source geometry using only scattered arrivals. (c) Schematic illustration of ray paths for obtained ghost scattered waves for virtual-source location at receiver 1 using the arrivals from (b). (d) Schematic ray paths for the active-source geometry using direct and scattered arrivals. (e) Schematic illustration of ray paths for retrieved physical scattered waves for virtual-source location at receiver 1 using the arrivals from (d). (For interpretation of the references to color in this figure legend, the reader is referred to the web version of this article.)

along an enclosing boundary. As we have only one source, we omit the summation over the sources. In Fig. 1a the acquisition geometry and the model parameters are given. Illustrative ray paths from the source to receivers for surface waves are shown in Fig. 1b. Selecting one of the receivers as the virtual-source location, here receiver 1, we cross-correlate each trace of the record with the trace at the virtual source by using Eq. (1). Physical surface wave are retrieved from the correlation of the direct arrival d^{VS} at receiver 1 with scattered arrivals d^i at all receivers (Fig. 1b; see also, e.g., Halliday and Curtis, 2009). The correlation process eliminates the traveltime for the

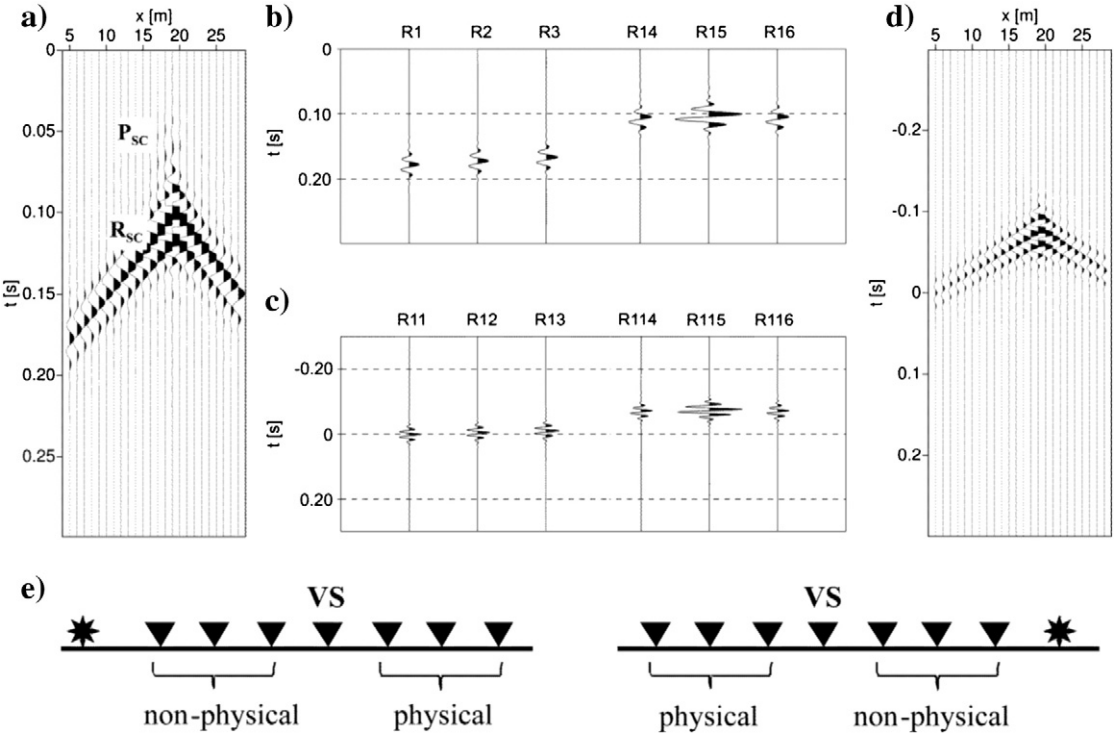

Fig. 2. (a) The modelled scattered wavefield: P_{SC} and R_{SC} denote the scattered P- and Rayleigh waves. (b) A closer view at the scattered arrivals at receivers R1–R3 and R14–R16. (c) Cross-correlation results for the traces in (b) for a virtual source at R1. (d) Total ghost scattered surface waves obtained by cross-correlation of the traces in (a) for a virtual source at R1. (e) Illustration of which receivers will have retrieved physical and non-physical arrivals with respect to the virtual-source position.

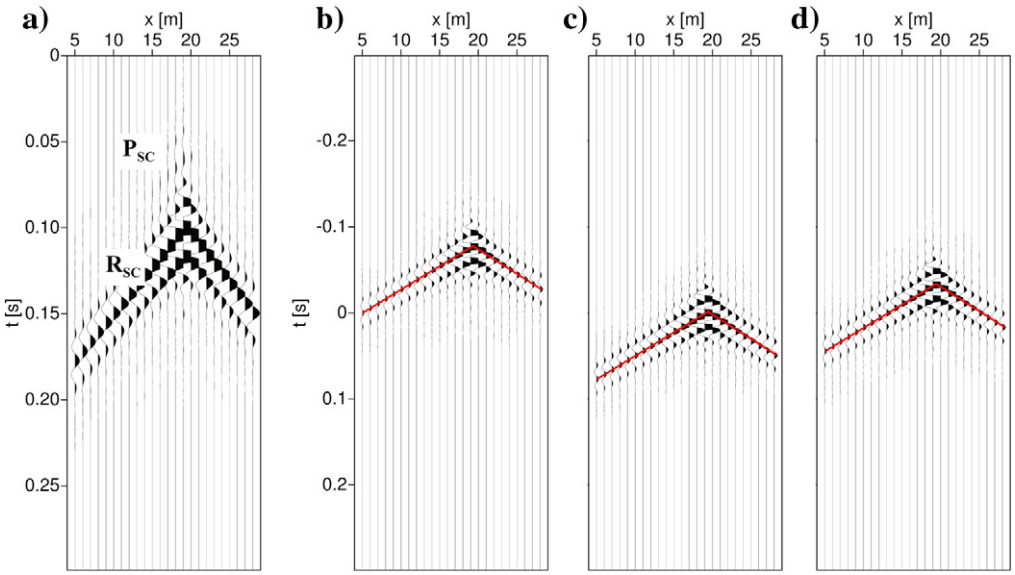

Fig. 3. (a) The modelled scattered wavefield in Fig. 2a. (b), (c) and (d): Ghost scattered surface waves retrieved by applying seismic interferometry to (a) for virtual source locations 1, 15 and 21 (5, 19 and 25 m), respectively.

common travel-path to receiver 1 (highlighted in red in Fig. 1b) and turns receiver 1 into a virtual source. We are left over with the green paths in Fig. 1c, which are the same as the paths that would be recorded by the receivers if there were a (virtual) source at the position of receiver 1. The retrieval of physical surface waves for our 2-D geometry is possible with Eq. (1) (that is, without the second summation over boundary of sources) because any source to the left of receiver 1 will be lying along the specular ray for scattered ways between receiver 1 and the rest of the receivers.

If we use Eq. (1) for the situation illustrated in Fig. 1d, i.e. for correlation of the scattered arrival at receiver 1 (highlighted in red) with the scattered arrivals at all receivers (shown in blue), we would retrieve ghost scattered surface waves. In this case, the correlation process eliminates the traveltime not only for the common travel-path from the source to receiver 1, but also for the path from the scatterer to receiver 1. In such a way, we are left over with traveltimes (at positive or negative times) that do not correspond to physical travel-paths. Such paths are illustratively indicated in Fig. 1e with the dashed green lines. Retrieval of ghost scattered body waves follows the same logic.

The scattered wavefield corresponding to the acquisition geometry of Fig. 1a is calculated for demonstration purposes by the method given in Kaslilar (2007); this method allows direct calculation of the scattered wavefield by considering contrast in density only (Fig. 2a). For the modelling, a cavity is considered and the parameters given in Fig. 1a are used. In Fig. 2a the scattered P- and Rayleigh waves are clearly observed. Using the shot record in Fig. 2a and the virtual-source location at receiver 1 (5 m), we explicitly show how we calculate the ghost scattered waves. For clarity of explanation, we show in Fig. 2b only the first three traces (receivers R1–R3, 5–7 m) and the traces above the scatterer (receivers R14–R16, 18–20 m). We cross-correlate each trace in the record (R1–R3 and R14–R16) with the trace at the receiver selected for a virtual source, in this example R1, and we obtain the

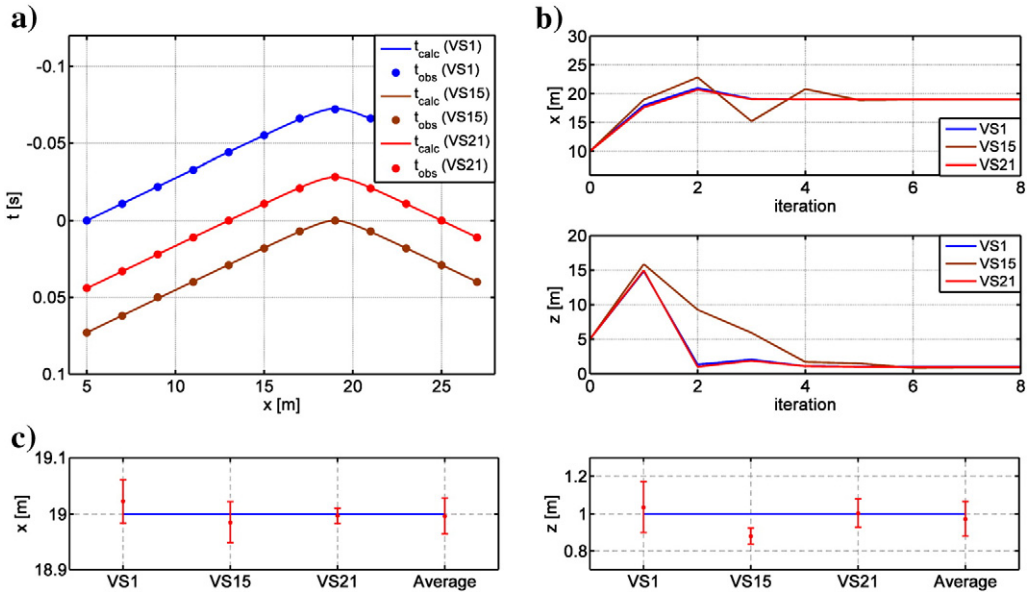

Fig. 4. (a) Observed (dots) and calculated (solid line) traveltimes; (b) estimated horizontal and vertical locations of the scatterer for the virtual sources 1 (blue, 5 m), 15 (brown, 19 m) and 21 (red, 25 m). The values at the zeroth iteration correspond to the initial parameters for the inversion. (c) Estimated model parameters and their 95% confidence limits, blue line shows the actual midpoint of the point scatterer. (For interpretation of the references to color in this figure legend, the reader is referred to the web version of this article.)

Table 1
The actual location (AL), the initial location (IL) for inversion and the estimated model parameters for different virtual-source (VS) locations for the model given in Fig. 1. E_t and E_m are the % errors of the traveltimes and model parameters calculated by Eqs. (8) and (9), respectively. σ_x and σ_z are standard deviations calculated from the diagonal of the model covariance matrix (Eq. (6)) and used in calculation of the 95% confidence levels (1.96σ).

	AL (m)	IL (m)	VS 1 (m)	E_m (%)	VS 15 (m)	E_m (%)	VS 21 (m)	E_m (%)	Averaged (m)	E_m (%)
x	19.00	10.00	19.022	0.11	18.985	0.08	18.997	0.01	18.996	0.02
z	1.00	5.00	1.035	3.50	0.880	12.00	1.003	0.30	0.972	2.80
$\mp\sigma_x$			0.0195		0.0185		0.0070		0.0162	
$\mp\sigma_z$			0.0687		0.0219		0.0379		0.0468	
E_t (%)			0.053		0.058		0.072			

interferometric record shown in Fig. 2c. The first obtained trace R11 is the result of correlating the trace at the first receiver with itself i.e., autocorrelation. Therefore the maximum amplitude is obtained at $t=0$, zero lag time. R12 is the cross-correlation of the traces R1 and R2. As is seen from the figure, the arrival times of the traces are shifted to the negative times. Continuing further, the correlation of the traces R1 and R14 results in the obtained trace R114, whose scattered arrival is at negative times. Repeating this procedure for each trace in the shot record we obtain the ghost scattered surface waves given in Fig. 2d. In this example, the dominant waveform is the surface wave, therefore the maximum correlation is obtained for this phase. If the body wave is of interest, first the scattered surface waves have to be removed and SI can be applied to the remaining body waves. With this application, cross-correlating two scattered wavefields at the receivers, we obtain ghost scattered surface or body waves.

To obtain physical scattered surface waves, we would need to correlate, as explained above, the direct arrival at d^{VS} with the scattered arrivals at d^i. Note that in this example the direct arrival is not modelled and thus physical scattered surface waves cannot be obtained. In the field, the direct arrival will, of course, be present. Even in this case, because the source is only to the left of the receivers, we would have a one-sided illumination and a physical scattered surface-wave arrival is obtained only when d^{VS} is to the left of d^i; for the reversed case the result is again non-physical (Fig. 2e).

Retrieval of physical scattered body waves is impossible for this model when the source and the receivers are at the surface. To retrieve the physical scattered body waves, the receivers will need to be placed between the source and the scatterer, for example in a borehole, and there will have to be multiple sources at the surface (see e.g. Schuster, 2009). If the modelled buried object is a point scatterer, it scatters the illuminating wavefield in the same way irrespective of the position of the surface source and the retrieved ghost scattered waves will be the same for any position of the surface source, except for the case when losses are present in the medium. In the latter case, the only

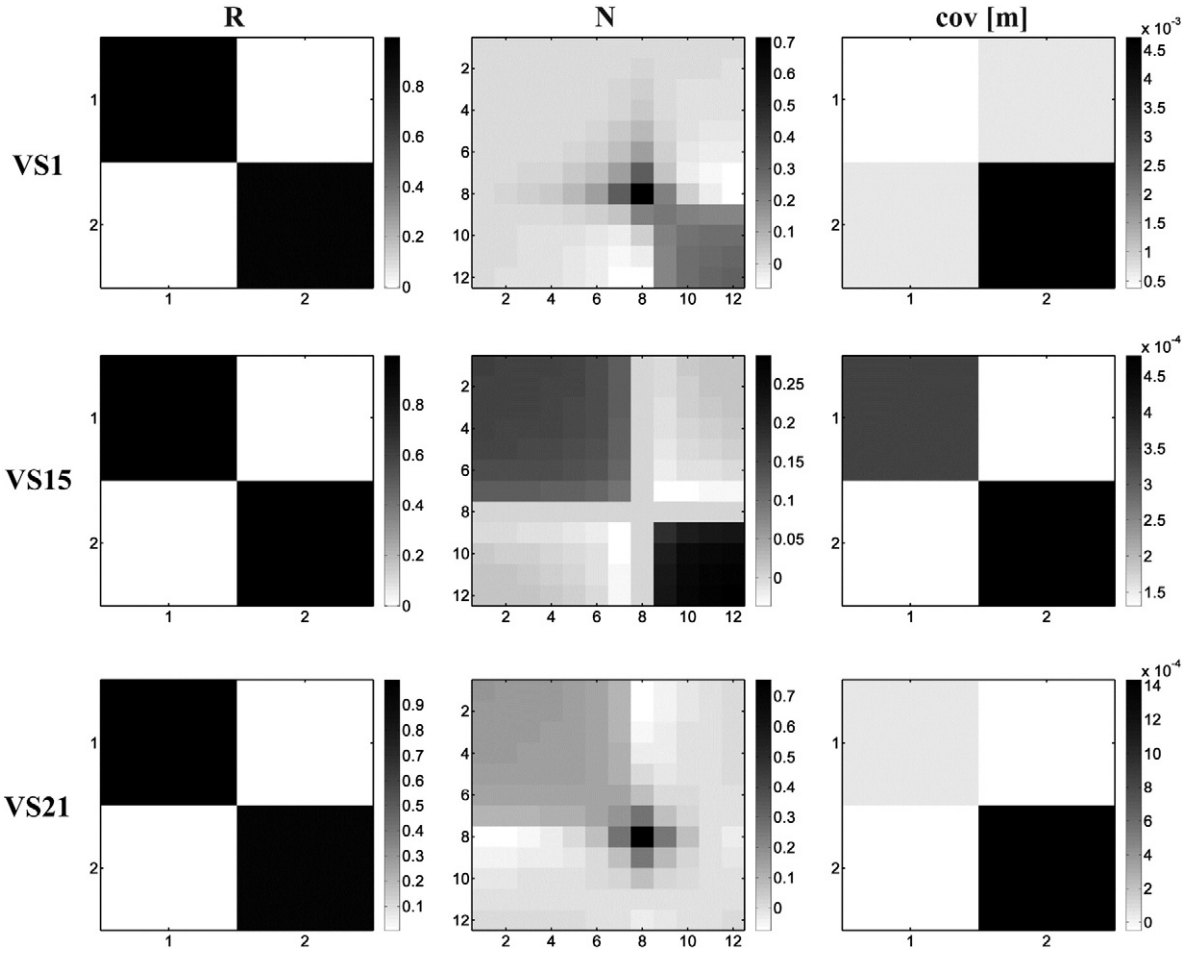

Fig. 5. The model resolution (**R**), data resolution (**N**) and model covariance (cov[**m**]) matrices for the virtual sources 1, 15 and 21. The model and data resolution matrices are dimensionless while the first and the second values on the diagonal of cov[**m**] corresponds to variances of the model parameters x[m^2] and z[m^2], respectively.

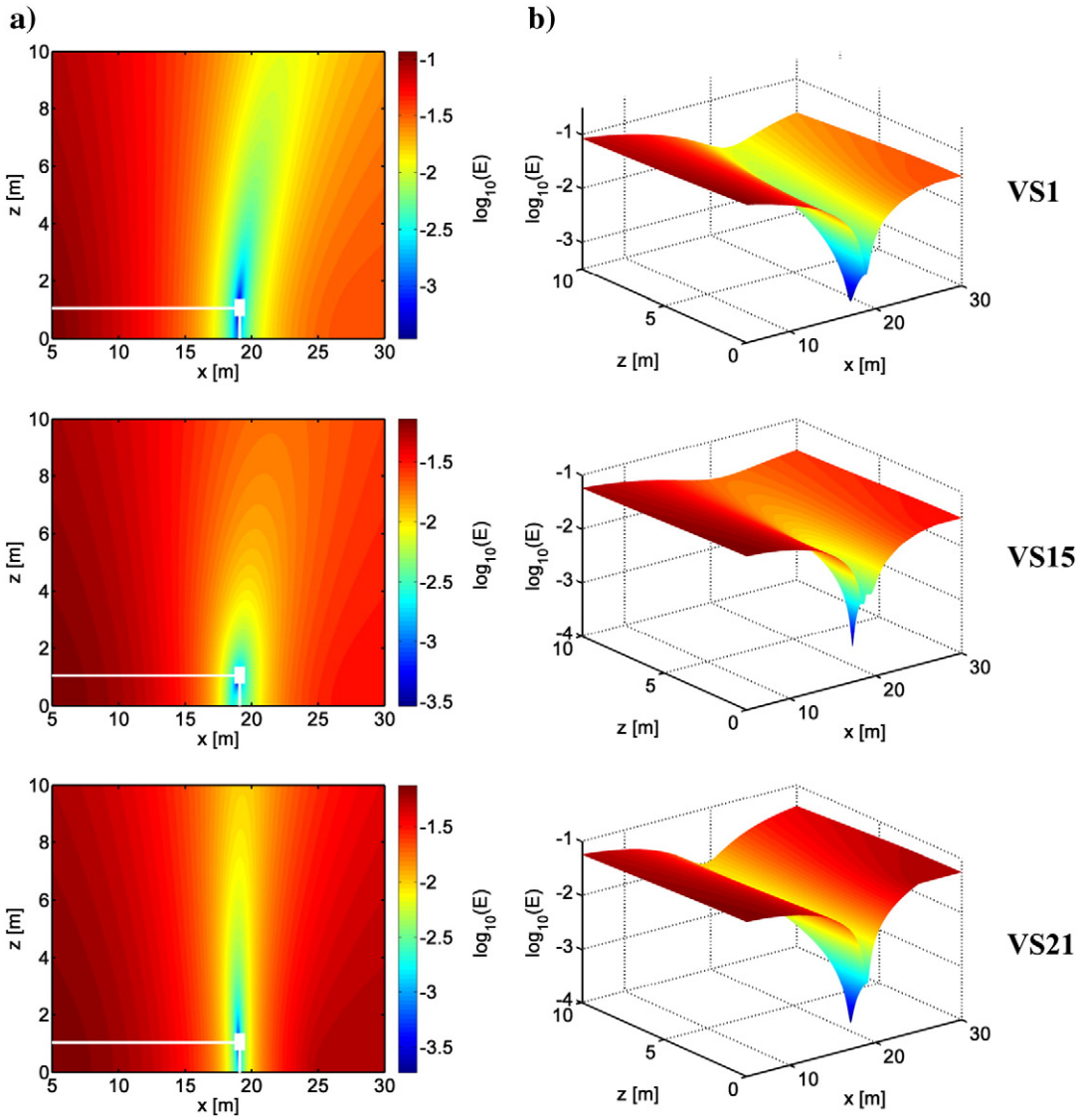

Fig. 6. Results of the grid search method for the model given in Fig. 1a and for virtual sources 1, 15 and 21 respectively. (a) 2D and (b) 3D illustration of the results. The white lines in (a) show estimated locations x and z corresponding to the minimum error, and the white boxes represent the location of the scatterer.

change in the retrieved ghost will be in its dominant frequency. For these reasons, when very few active sources are available, and in our extreme example — only one, it is more practical to use retrieved ghost scattered waves.

2.2. Estimating the location of the scatterer using inversion

To estimate the location of the scatterer, the following theoretical ghost traveltime relation is used:

$$t_i = \frac{1}{V}\left\{\left[(x_i^r - x)^2 + (z_i^r - z)^2\right]^{1/2} - \left[(x_{vs} - x)^2 + (z_{vs} - z)^2\right]^{1/2}\right\}. \quad (2)$$

The relation gives the retrieved ghost traveltimes between the virtual source, the scatterer and the receivers (Fig. 1c). In the equation, V is the wave velocity, i is the index for the receiver numbers, r and vs denote the receiver and the virtual source, while x and z are the location of the scatterer in the horizontal and vertical direction, respectively.

In all examples of this paper, the wave velocity is considered as known and it is estimated from the direct arrivals of the shot record, and the origin of the coordinate system is chosen at the active-source position. To find the location of the scatterer, the traveltime relation (Eq. (2)) and the traveltimes obtained for each virtual-source location are used in the inversion. The nonlinear problem is solved iteratively. The system of equations for the forward problem is denoted as $\Delta\mathbf{d} = \mathbf{G}\Delta\mathbf{m}$. In this relation, the difference between the observed t_{obs} (retrieved), and the calculated t_{calc} (Eq. (2)) ghost scattered data is denoted by $\Delta\mathbf{d} = t_{obs} - t_{calc}$, the unknown model parameters — the horizontal x and vertical z locations of the scatterer — are denoted by the vector $\Delta\mathbf{m}$, while the Jacobian matrix is represented by $\mathbf{G}$. The damped least-squares solution of the inverse problem is given in terms of Singular Value Decomposition (SVD) as

$$\Delta\mathbf{m} = \mathbf{V}\boldsymbol{\Lambda}\left(\boldsymbol{\Lambda}^2 + \beta^2\mathbf{I}\right)^{-1}\mathbf{U}^T\Delta\mathbf{d}, \quad (3)$$

Table 2
Comparison of the results of the inversion (SVD) and grid search (GS) method. The last row shows the errors in traveltime calculated by Eq. (8).

	Actual Location	VS 1 (SVD)	VS 1 (GS)	VS 15 (SVD)	VS 15 (GS)	VS 21 (SVD)	VS 21 (GS)
x [m]	19.00	19.022	19.02	18.985	18.98	18.997	19.00
z [m]	1.00	1.035	1.035	0.880	0.880	1.003	1.005
E_t (%)		0.053	0.053	0.058	0.059	0.072	0.073

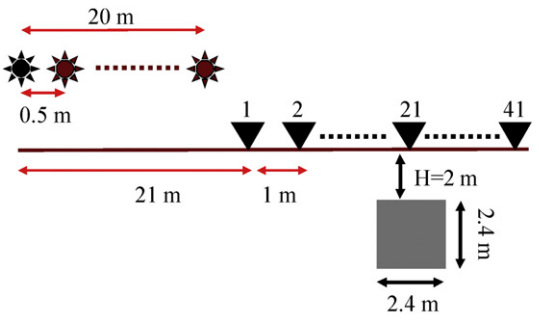

	Background	Scatterer
ρ [kg/m³]	1800	1000
V_p [m/s]	700	400
V_s [m/s]	400	170

Surface wave velocity [m/s]	360
Dominant frequency [Hz]	200
Dominant wavelength [m]	1.80

Fig. 7. Schematic view of the model (left): The sources (stars), receivers (triangles) and scatterer (gray square). The modelling parameters are given in the table (right).

where $\mathbf{V}$,$\mathbf{\Lambda}$,$\mathbf{U}$,$\mathbf{I}$ and β are the model-space eigenvectors, the diagonal matrix containing the eigenvalues, the data-space eigenvectors, the identity matrix and the damping parameter, respectively. The damping parameter is chosen as the lowest non-zero singular value (Xia et al., 2010). Considering Eq. (3), the inverse problem is solved to find the location of the scatterer.

To assess the quality of the inversion results, the data resolution ($\mathbf{N}$), the model resolution ($\mathbf{R}$) and the model covariance (cov[$\mathbf{m}$]) matrices including the damping parameter are calculated by using the following relations (Randall and Zandt, 2007):

$$\mathbf{N} = \mathbf{U}\mathbf{\Lambda}^2\left(\mathbf{\Lambda}^2+\beta^2\mathbf{I}\right)^{-1}\mathbf{U}^T, \tag{4}$$

$$\mathbf{R} = \mathbf{V}\mathbf{\Lambda}^2\left(\mathbf{\Lambda}^2+\beta^2\mathbf{I}\right)^{-1}\mathbf{V}^T, \tag{5}$$

$$\mathrm{cov}[\mathbf{m}] = \sigma^2\mathbf{V}\mathbf{\Lambda}^2\left(\mathbf{\Lambda}^2+\beta^2\mathbf{I}\right)^{-1}\mathbf{V}^T, \tag{6}$$

where

$$\sigma^2 = \frac{1}{n-n_m}\sum_{i=1}^{n}(t_{obs}-t_{calc})^2. \tag{7}$$

In Eq. (7), n is the number of observed data and n_m is the number of model parameters (here $n_m=2$). In our examples, the uncertainties of the estimated parameters are calculated with a coverage factor 2, providing a level of 95% confidence (1.96σ), and plotted with the estimated model parameters for each selected virtual source.

To show the estimation procedure, we use the scattered wavefield given in Section 2, Fig. 2a. The direct Rayleigh waves, which dominate the interferometric image, are not present in the wavefield and the traveltimes of the interferometric estimate corresponding to ghost scattered surface waves are easily selected.

Fig. 3a–d shows the shot record given in Fig. 2a and the obtained interferometric scattered waves for the virtual-source locations 1, 15 and 21 (5, 19, 25 m), respectively. As the virtual source at receiver 1 is to the left of the receivers 2–24, the obtained wavefield after SI is at negative times (Fig. 3b). When the virtual source position is at the top of the scatterer, receiver 15, the obtained scattered arrival at the virtual source are at $t=0$ s and the rest of the arrivals at positive times, (Fig. 3c). When the virtual source is at receiver 21, again the scattered wavefield at the virtual source is at $t=0$ s, some of the arrivals are at negative times and most arrivals at positive times. It can be seen from Fig. 3b–d that the scattered fields are the same, except for a shift along the time axis. This time shift depends on the distance from the virtual source to the scatterer only. Change in

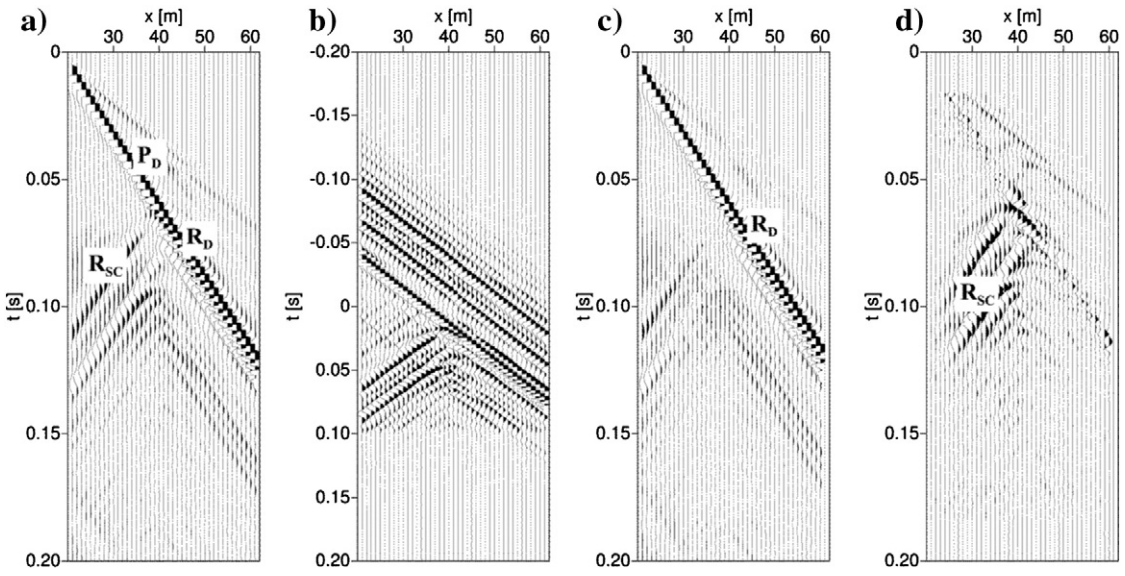

Fig. 8. (a) Shot gather which is designated for removal of the direct surface wave. P_D, R_D and R_{SC} denote the direct P, direct Rayleigh and scattered Rayleigh waves. (b) Interferometric result for virtual-source location at receiver 1 without removal of the direct surface waves, (c) interferometric result with predictive filtering. (d) Shot gather with suppressed direct surface waves.

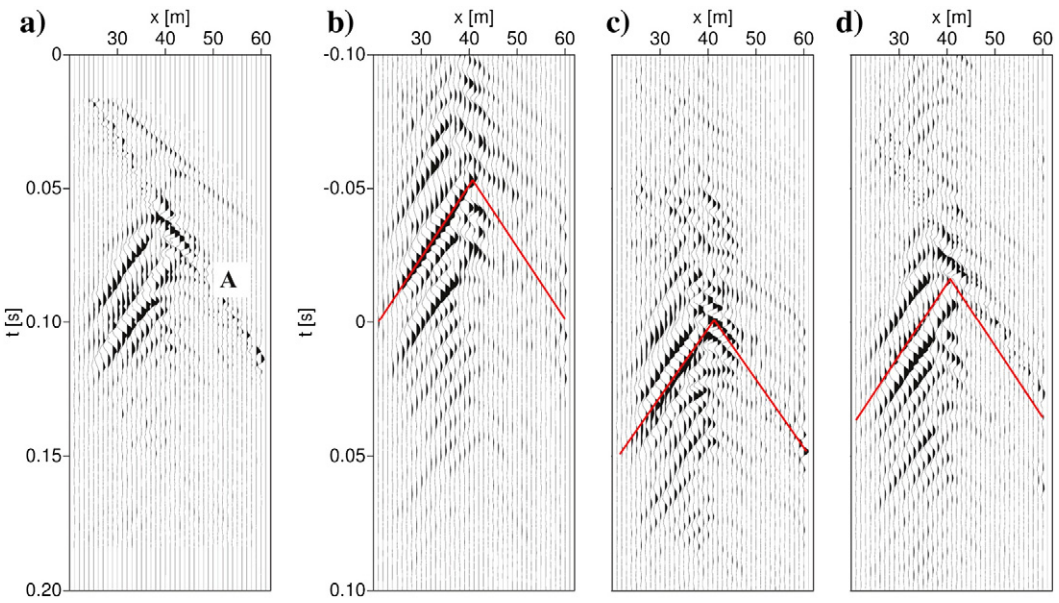

Fig. 9. (a) Estimated scattered wavefield. (b), (c) and (d): Ghost scattered surface waves retrieved by applying seismic interferometry to (a) for virtual source locations at receivers 1, 21 and 30 (21, 41 and 50 m), respectively.

the lateral direction of the medium parameters to the left and to the right of the receiver array will not affect the retrieved ghost traveltimes.

To find the location of the scatterer, the ghost traveltimes are picked from the maximum amplitude of the retrieved ghost scattered surface waves. The picked traveltimes are shown by the red lines on Fig. 3b–d. The traveltime relation (Eq. (2)) and the traveltimes obtained for each virtual-source location are used in the inversion. Considering Eq. (3), the inverse problem is solved to find the location of the scatterer. The best fit between the observed and calculated traveltimes of the ghost scattered surface waves for virtual sources 1, 15 and 21 (5 m, 19 m and 25 m) are given in Fig. 4a.

It can be seen that there is a good agreement between the observed and the calculated traveltimes of the ghost scattered surface waves. The agreement can be quantified by the following relation:

$$E_t = \frac{\sum_{i=1}^{N} (t_{obs} - t_{calc})^2}{\sum_{i=1}^{N} t_{calc}^2} x100 \quad . \tag{8}$$

The calculated error E_t for the virtual-source locations are given in Table 1, and they are less than 1%. The initial (also given in Table 1)

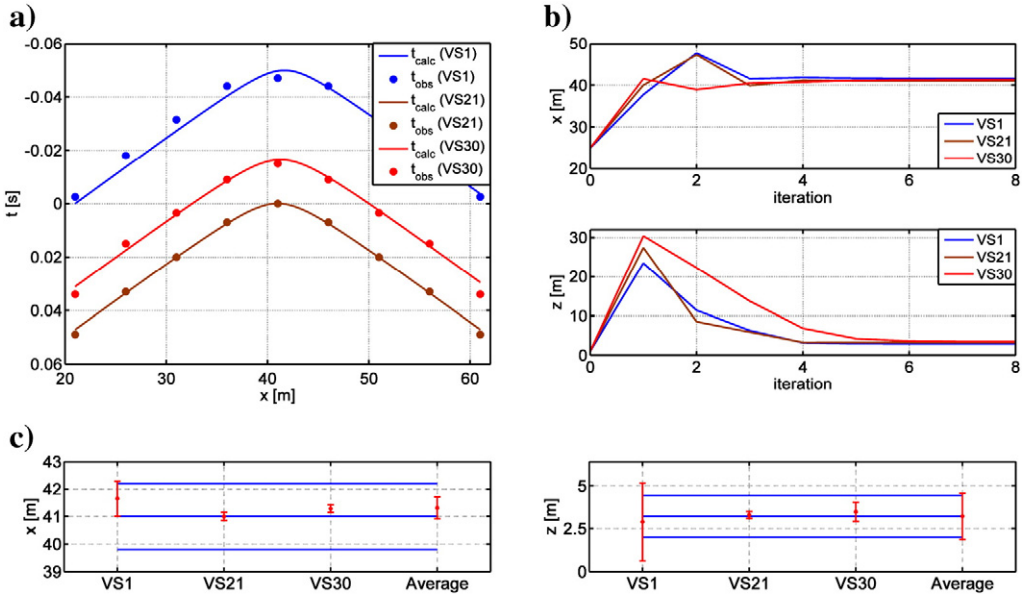

Fig. 10. (a) Observed (dots) and calculated (solid line) traveltimes; (b) estimated horizontal and vertical location of the scatterer for virtual sources 1 (blue, 21 m), 21 (brown, 41 m) and 30 (red, 50 m). The values at the zeroth iteration correspond to the initial parameters for the inversion. (c) Estimated model parameters and their 95% confidence limits, blue lines show the actual midpoint and the left/right (x) and upper/lower (z) bounds of the scatterer. (For interpretation of the references to color in this figure legend, the reader is referred to the web version of this article.)

Table 3
The actual location (AL), the initial location (IL) for inversion and the estimated model parameters for different virtual source (VS) locations for the model given in Fig. 7. E_t and E_m are the % errors of the traveltimes and model parameters calculated by Eqs. (8) and (9), respectively. σ_x and σ_z are standard deviations calculated from the diagonal of the model covariance matrix (Eq. (6)) and used in calculation of the 95% confidence levels (1.96σ).

	AL (m)	IL (m)	VS 1 (m)	E_m (%)	VS 21 (m)	E_m (%)	VS 30 (m)	E_m (%)	Averaged (m)	E_m (%)
x	41.00	25.00	41.65	1.6	41.00	0.0	41.28	0.68	41.31	0.76
z	3.20	1.00	2.89	9.7	3.28	2.5	3.47	8.4	3.21	0.4
$\mp\sigma_x$			0.3300		0.0780		0.0690		0.2024	
$\mp\sigma_z$			1.1600		0.1030		0.2820		0.6919	
E_t (%)			0.9449		0.0319		0.1374			

and the updated model parameters after each iteration are given in Fig. 4b. As stopping criteria for the iterations, we use a fixed iteration number for each model. This number is fixed when the changes in the model parameters become less than 0.1%. In this example, after six iterations, the model parameters, the horizontal and vertical location of the scatterer, get close to the actual values. In Fig. 4c the estimated parameters and their 95% confidence intervals, obtained by Eq. (6) are shown, for each of the used virtual-source location. The last value in Fig. 4c is the average over the results for the different virtual sources. The blue line in Fig. 4c represents the actual midpoint of the point scatterer. In this example, both the horizontal and vertical location of the scatterer are well estimated.

The errors in the estimated model parameters are calculated by

$$E_m = \left|\frac{m_{act} - m_{est}}{m_{act}}\right| \; x \; 100 \;, \tag{9}$$

where m_{act} and m_{est} are the actual and estimated model parameters (x or z), respectively. For all virtual source positions, it is observed that the errors of the estimated model parameters (x and z) are less than 12%. The average of the estimated values are calculated to be $x = 19.99$ and $z = 0.97$, meaning errors 0.02% and 2.80% respectively, which are obtained by considering error propagation rules.

The images of the resolution and covariance matrices are given in Fig. 5. It should be emphasized that the images of these matrices are only illustrated for this modelling example. For the other models considered in the following sections, similar results are obtained. It can be seen in Fig. 5 that for the three virtual-source locations, the diagonal of the model resolution matrix ($\mathbf{R}$) is close to identity matrix ($\mathbf{m^{act} = R\, m^{est}}$), which indicates very good resolution or estimation of the actual model parameters (x and z). The best data resolution can be achieved if the data resolution matrix is unity. Here, the values of the data resolution matrix ($\mathbf{N}$) are around the diagonal; however, it is not the identity matrix. That means the predicted data, d^{pre}, are weighted averages of the observed data d^{obs}, ($\mathbf{d^{pre} = N\, d^{obs}}$). For example, the rows of the data resolution matrix $\mathbf{N}$ for VS1 (Fig. 5) weigh the observed data ${d_{1-6}}^{obs}$ with weights close to zero. The observed data at receivers 1–6 correspond to the shortest interferometric traveltimes. The predicted data ${d_8}^{pre}$ is weighted with the highest weight of $\mathbf{N}(8,8)$ in the middle and has the largest effect on the

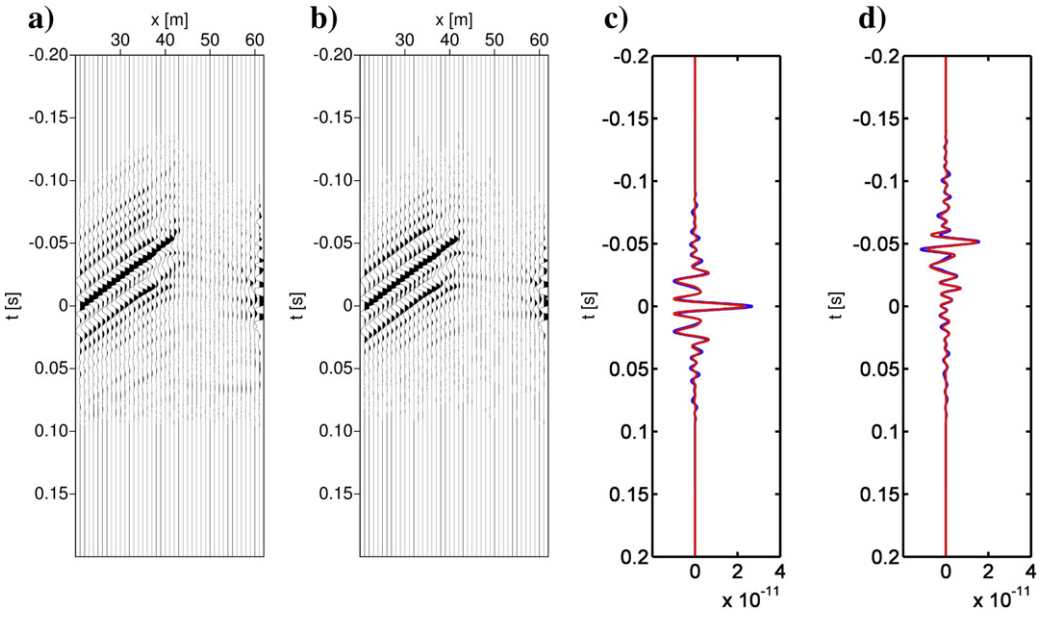

e)

	Actual Location	Single shot	Summed five shots
x [m]	41.00	41.049	41.046
z [m]	3.20	3.450	3.443

Fig. 11. Retrieved ghost scattered surface waves from (a) a single shot and (b) after summation of correlation results from five shots. Comparison of the retrieved traces for (c) receiver location at 21 m and for (d) receiver location 40 m, from the panel in (a) (blue color) and the panel in (b) (red color). (e) Estimated location of the scatterer for the single-shot and five-shots results. (For interpretation of the references to color in this figure legend, the reader is referred to the web version of this article.)

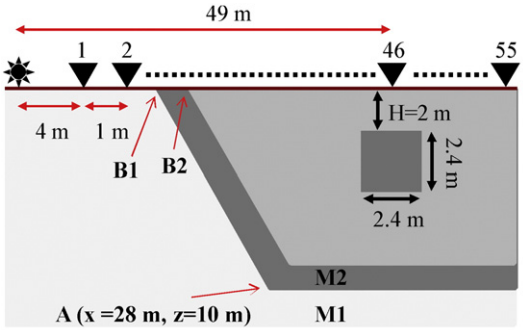

	M1	M2	Background	Scatterer
ρ [kg/m³]	1500	1500	1800	1000
V_p [m/s]	800	500	700	400
V_s [m/s]	500	300	400	170

Surface wave velocity [m/s]	360
Dominant frequency [Hz]	200
Dominant wavelength [m]	1.80

Fig. 12. Schematic view of the laterally inhomogeneous model (left): the source (star), receivers (triangles) and scatterer (gray square). The letter A indicates the corner of the low-velocity zone; B1 and B2 represent the two interfaces between the source and the receivers. M1 and M2 represent the media having different velocities. The modelling parameters are given in the table (right). The surface wave velocity, dominant frequency and wavelength correspond to the background medium of the scatterer.

data solution. This point is above the scatterer. Data between receivers 9 and 12, $d_{9-12}{}^{obs}$, are weighted with the rows 9–12 of the data resolution matrix. The data resolution matrix corresponding to VS15 has nearly zero values at the location of the scatterer. This point also corresponds to the shortest interferometric traveltime. Similar results are also obtained for the VS21.

2.3. Estimation of the location of the scatterer by the grid search method

The grid search method is used as a complementary method to estimate the horizontal and vertical location parameters. Here, Eq. (2) is calculated for a range of values for both x and z. Error function (difference between observed and calculated traveltimes) is calculated using

$$E = \sqrt{\frac{\sum_{i=1}^{N} (t_{obs} - t_{calc})^2}{N}}, \tag{10}$$

where N is the number of observation points. The minimum of the errors give the best fit for x and z parameters. In Fig. 6, the log errors are plotted as 10-base logarithm. The location of the scatterer is represented by the white square and the white lines to the axes x and z represent the estimated values corresponding to the minimum errors.

The estimated results for the inversion and grid search methods are given in Table 2. The model parameters estimated with grid search method are very close to the ones estimated with the inversion. In the last row of Table 2 are given the errors in the model parameters calculated by Eq. (8) for both methods.

3. Data from finite-difference modelling of the wavefield

To test the proposed method with realistic subsurface models, recordings are produced by the elastic 2D finite-difference modelling program from Thorbecke and Draganov (2011). The generated data are vertical-component velocity recordings. Here, two different models are considered. In the first one, a scatterer is located in a half space. In this model, we generate many inline shot gathers and compare the estimations of the location of the scatterer in case only one active-shot position is used and in case the retrieval is performed by summing the cross-correlation results from several active shots. Furthermore, the surface waves dominate the recordings and elimination of these waves becomes necessary before the application of the method. When many shot gathers are available, interferometric prediction and subtraction of surface waves can be used as an alternative to f–k (frequency–wavenumber) filtering for the elimination of the surface waves from the modelled data. In the second model, we include lateral inhomogeneity and estimate the location of a corner diffractor and a scatterer

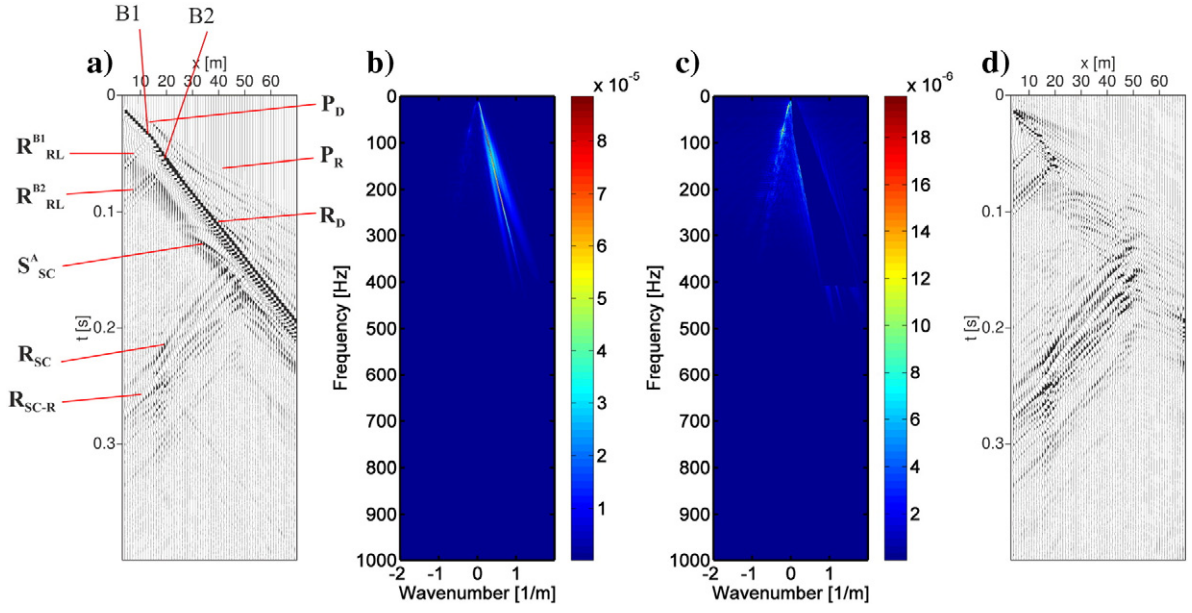

Fig. 13. (a) Shot gather for the model given in Fig. 12. The labels for the various arrivals are explained in Table 4. f–k domain representation of the data (b) before and (c) after the removal of direct surface waves and fast arrivals. (d) The gather from a) after f–k filtering.

Table 4
List of the labelled arrivals in the modelled shot gather given in Fig. 13a.

P_D	Direct P
P_R	Refracted P
R_D	Direct Rayleigh
R_{SC}	Scattered Rayleigh
R_{SC-R}	Scattered and Refracted Rayleigh
S^A_{SC}	Scattered S wave from A
R^{B1}_{RL}	Reflected Rayleigh from B1
R^{B2}_{RL}	Reflected Rayleigh from B2

by using scattered body and surface waves, respectively. We show the effectiveness of the method in the case of lateral variations in the medium.

3.1. Scatterer in a half space

The model consists of a scatterer placed below the surface in a half space. The geometry and the medium parameters of the model, which represent a realistic near-surface structure, are given in Fig. 7. A total of 41 shot gathers are obtained by shifting the source location closer to the scatterer by 0.5 m while keeping the receivers fixed. Fig. 8a shows the shot gather for a shot placed at 1 m from receiver 1. The direct P (P_D) and Rayleigh (R_D) waves, and the scattered Rayleigh (R_{SC}) waves are clearly observed in the figure.

To compare the estimation of the location of the scatterer we use the result from a single shot with results for summed five shots. Since the direct surface waves in these recordings tend to mask the ghost scattered waves in the SI result (Fig. 8b), the estimation of the scattered wavefield is necessary. In the following subsection, the scattered wavefield is obtained by using interferometric prediction and subtraction of surface waves as proposed by Dong et al. (2006). In the rest of the models, we use *f–k* filtering for the suppression of the direct surface wave.

3.1.1. Estimating the location of the scatterer using a single active source

Adapting the code given in Schuster (2009) for our purpose, the direct Rayleigh waves from a selected shot gather are eliminated by interferometric prediction and subtraction (Dong et al., 2006). The first 20 shots are used since the best estimation is obtained by these shot gathers. Using predictive filtering, the direct surface waves in the SI result is matched with the direct surface waves in a selected shot gather. Since the direct surface waves are the dominant components in either images, the predictive filtering matches the amplitude and phase of the direct surface waves. Finally, the matched interferometric image (Fig. 8c) is subtracted from the selected shot gather (Fig. 8a), leaving a shot gather dominated by the scattered surface waves (Fig. 8d).

SI is then applied to the estimated scattered waves (Fig. 8d) using the procedure described in Section 2.2. In Fig. 9a we show the estimated scattered wavefield, while in Fig. 9b–d the retrieved ghost scattered surface waves for virtual sources at receivers 1, 21 and 30, respectively (21, 41 and 50 m) are shown within the intervals −0.1 and 0.1 s. Compared with the SI results of the undisturbed scattered wavefields from the previous section (Fig. 3), these ones are somewhat more complex due the presence of direct surface-wave remnants and other artefacts.

In this model, there are two points that have to be considered: *i*) the elimination of direct surface waves also eliminates the right branch of the scattered field, which has nearly the same slope and frequency content as the direct surface wave. Therefore picking the traveltimes on the right branch is mostly not possible or confident (A in Fig. 9a). *ii*) When the scatterer is not close to a point scatterer, besides scattering, the wavefield at the scatterer will also undergo reflection and refraction and will exhibit directionality. Therefore, the right-hand side of the scattered branch will have different slopes. In this case, Eq. (2) will not be a good model, since it is valid for a point scatterer. However, the corner of the scatterer will still generate scattered wavefields and these can be used for location purposes. In both cases *i* and *ii*, knowing the apex of the scattered wavefield, which can also be approximately determined from a clear shot gather, and the traveltimes at one side of the scattering hyperbola (here, left-side branch, since the source is at the left), we can extrapolate for the opposite branch by taking the symmetry of the scattering hyperbola and use it for the estimations of the locations.

Using the ghost-traveltime relation from Eq. (2) and SVD for inversion by Eq. (3), location of the scatterer is estimated using the same method as described in Section 2.2. The best fit between the observed and calculated traveltimes of the ghost scattered surface waves for virtual sources 1, 21 and 30 (21, 41 and 50 m) are given in Fig. 10a. The initial (also given in Table 3) and the updated model parameters after each iteration are given in Fig. 10b. In Fig. 10c are shown the estimated model parameters together with their 95% confidence intervals, calculated by Eq. (6), for each of the used virtual-source locations. The last value in Fig. 10c is the average

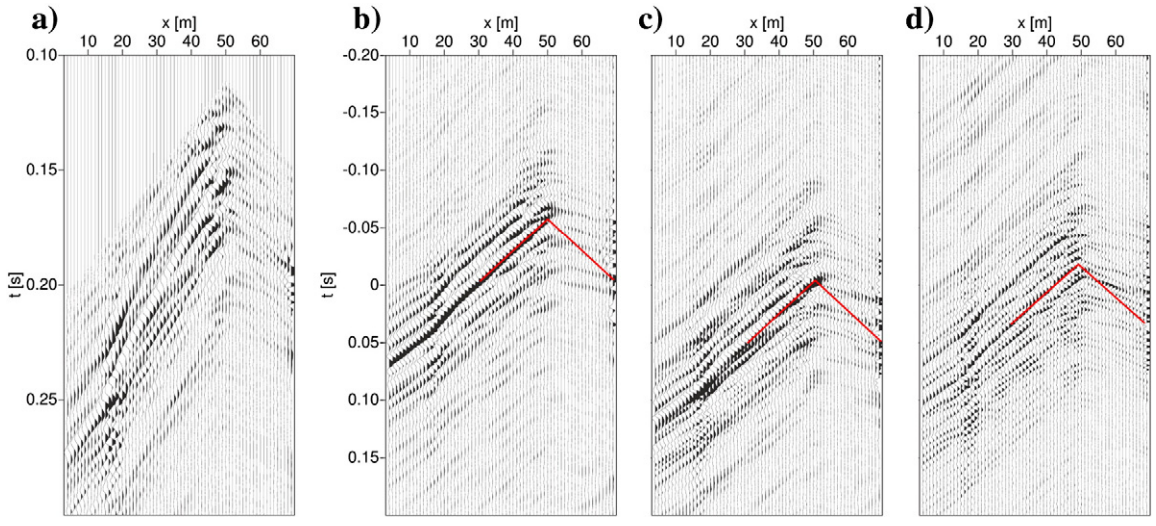

Fig. 14. (a) Extracted scattered surface waves from the panel in Fig. 13d for traveltimes between 0.1 and 0.3 s. Ghost scattered surface waves retrieved by applying seismic interferometry to (a) for virtual-source locations at receivers (b) 26 (29 m), (c) 46 (49 m) and (d) 55 (58 m).

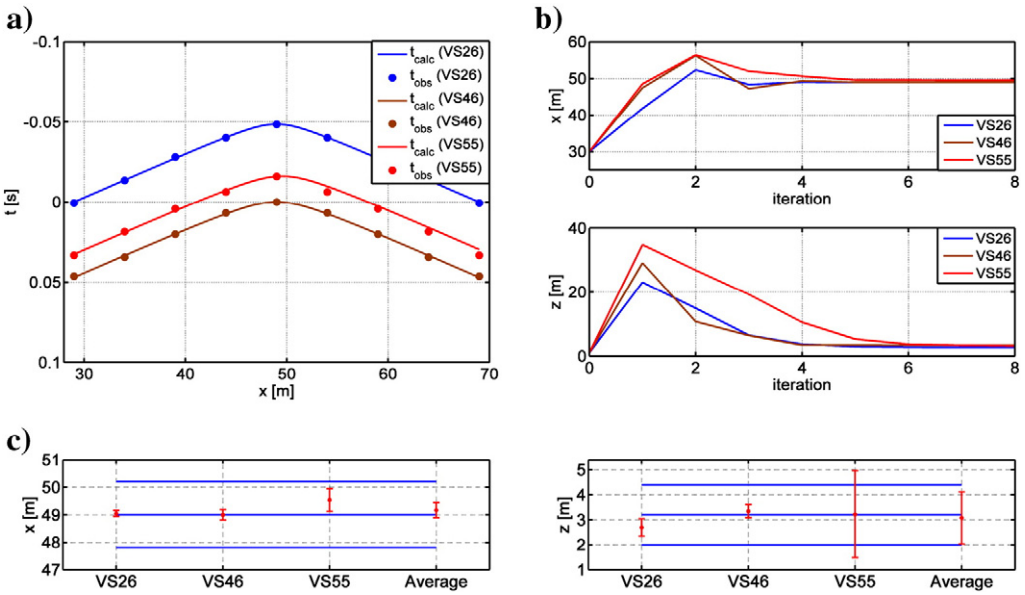

Fig. 15. (a) Observed (dots) and calculated (solid line) traveltimes; (b) estimated horizontal and vertical locations of the scatterer for the virtual sources 26 (blue, 29 m), 46 (brown, 49 m) and 55 (red, 58 m). The values at the zeroth iteration correspond to the initial parameters for the inversion. (c) Estimated model parameters and their 95% confidence limits, blue lines show the actual midpoint and the left/right (x) and upper/lower (z) bounds of the scatterer. (For interpretation of the references to color in this figure legend, the reader is referred to the web version of this article.)

over the results for the different virtual sources; the blue lines represent the actual midpoint, the actual left/right (x) and upper/lower (z) bounds of the scatterer.

For all virtual source positions, it is observed that the errors (Eq. (9)) of the estimated model parameters (x and z) are less than 10%, which is similar to the previous example (Table 3). The average of estimated values are calculated as x = 41.31 and z = 3.21 meaning errors 0.76%, 0.4% respectively.

3.1.2. Estimating the location of the scatterer using summation over several active source

In Fig. 11a we repeat the retrieved ghost scattered surface waves from Fig. 9b for a virtual source at receiver 1. Fig. 11b shows the result after summing the retrieved scattered surface waves obtained from shot gathers from active sources at locations 1 m, 11 m, 21 m, 31 m and 41 m. The direct P- and Rayleigh waves are removed by f–k filtering before cross-correlation. The retrieved results in Fig. 11a and b are similar, except for some high-frequency oscillations present in the single-shot result. These oscillations are especially notable around the time interval −0.10 s to −0.05 s, when compared to the summed SI result in Fig. 11b. For comparison, the traces of the single-shot (Fig. 11a) and the summed-shot results (Fig. 11b) for receivers 1 (21 m) and 20 (40 m) are given in Fig. 11c and d, respectively. We see that the difference between the summed (red line) and single-shot (blue-line) traces is the elimination of the high-frequency oscillations at the sides of the main signal. In the table given in Fig. 11e it can be seen that the estimated results are very close for both cases, since the summation does not affect significantly the traveltimes of retrieved ghost scattered wavefield. In this sense, the method we propose is efficient, since a single shot is sufficient for estimating the location of the scatterer.

3.2. Laterally inhomogeneous model

To test the proposed method on a more complex model, we run the finite-difference modelling code for the geometry and medium parameters as given in Fig. 12. Fig. 13a shows the obtained shot gather and the abbreviations used in the figure are given in Table 4. In this model, we try to estimate the location of the scatterer from scattered surface waves and the location of the corner diffractor (indicated by A in Fig. 12) from body waves, namely diffracted S-wave, which is indicated by S_{sc}^{A} in Fig. 13a.

Similar to the previous section, removal of the direct Rayleigh waves is necessary before starting the retrieval of the ghost waves. However, since there is only one shot gather available, the interferometric prediction of surface waves is not possible. Instead, an f–k filter is used to remove most of the direct Rayleigh waves and fastest arrivals (direct and refracted P-waves). Fig. 13b shows the f–k domain representation of the shot gather in Fig. 13a. After filtering the direct surface waves and the fastest arrivals (Fig. 13c) and transforming back to the t–x (time–distance) domain (Fig. 13d), the scattered wave field is obtained. To be able to follow the arrival times clearly, a zoomed view of the scattered wavefield is shown in Fig. 14a.

In Fig. 14b–d the retrieved ghost scattered surface waves for virtual-source locations at receivers 26, (left of the scatterer, 29 m), 46 (at the top of the scatterer, 49 m) and 55 (to the right of the scatterer, 58 m) are given, respectively. To have a closer look at the obtained ghost scattered surface waves, the correlation results are

Table 5
The actual location (AL), the initial location (IL) for inversion and the estimated model parameters for different virtual source (VS) locations for the scatter given in Fig. 12. E_t and E_m are the % errors of the traveltimes and model parameters calculated by Eqs. (8) and (9), respectively. σ_x and σ_z are standard deviations calculated from the diagonal of the model covariance matrix (Eq. (6)) and used in calculation of the 95% confidence levels (1.96 σ).

	AL (m)	IL (m)	VS 26 (m)	E_m (%)	VS 46 (m)	E_m (%)	VS 55 (m)	E_m (%)	Averaged (m)	E_m (%)
x	49.00	30.00	48.99	0.02	49.00	0.0	49.54	1.10	49.17	0.35
z	3.20	1.00	2.67	16.5	3.35	4.68	3.22	0.62	3.08	3.75
$\mp\sigma_X$			0.054		0.099		0.210		0.1381	
$\mp\sigma_Z$			0.193		0.130		0.886		0.5294	
E_t (%)			0.0293		0.0512		1.2428			

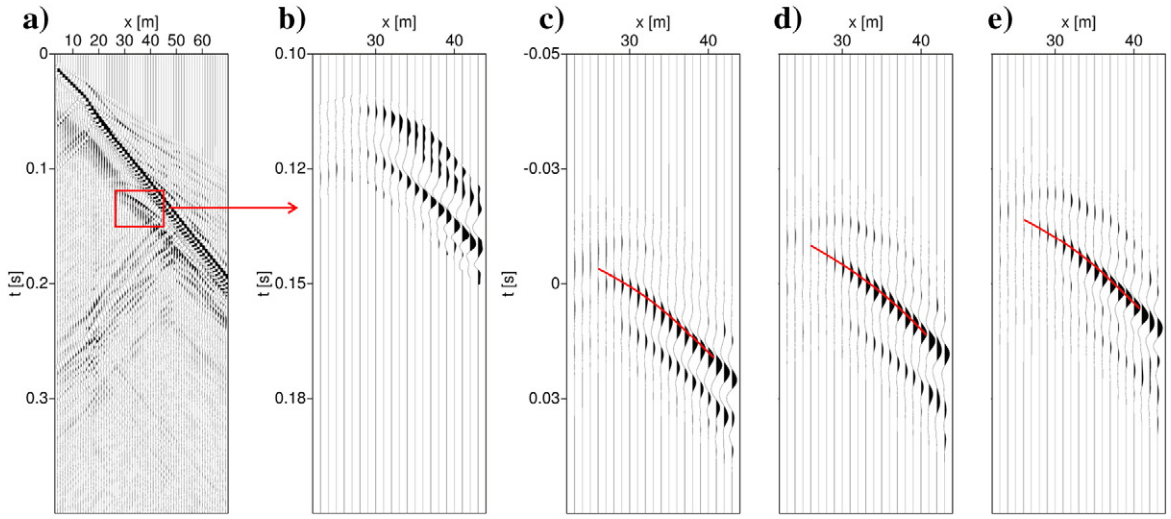

Fig. 16. (a) Shot gather for the model given in Fig. 12. (b) Extracted scattered S-wave from the shot gather in (a) (red box). Ghost scattered S-wave retrieved by applying seismic interferometry to (b) for virtual-source locations at receivers (c) 26 (29 m), (d) 30 (33 m) and (e) 34 (37 m). (For interpretation of the references to color in this figure legend, the reader is referred to the web version of this article.)

plotted between −0.2 and 0.2 s. Due to the *f*–*k* filtering, the right branch of the scatterer is filtered-out. We pick the traveltimes from the left branch of the scattered wavefield until the apex of the scattering hyperbola. For the right-hand side, we consider the scatterer as a point scatterer and use the traveltimes of the left part. The obtained traveltimes are used in the inversion for the location of the scatterer. The selected ghost traveltime curves are shown in red in Fig. 14b–d.

The location of the scatterer is estimated again by the method from Section 2.2, using the ghost traveltime relation Eq. (2) and SVD for inversion by Eq. (3). The best fit between the observed and calculated traveltimes of the ghost scattered surface waves for virtual sources 26, 46 and 55 (29, 49 and 58 m) are given in Fig. 15a and the initial (also given in Table 5) and the updated model parameters for each iteration are given in Fig. 15b. In Fig. 15c the estimated model parameters and their 95% confidence limits, obtained by Eq. (6) are shown, for each of the used virtual-source location. The last value is the average of the individual results. The blue lines in Fig. 15c represent the actual midpoint, the actual left/right (x) and upper/lower (z) bounds of the scatterer. In this example, both the horizontal and vertical locations of the scatter are well estimated and they are inside the boundaries of the scatterer. The estimated model parameters, together with their standard deviation, calculated by Eq. (6), and % error (Eq. (9)), are given in Table 5. Taking the average from the estimated values, we obtain $x = 49.17$ m and $z = 3.08$ m, whose errors are 0.35% and 3.75%, respectively.

To find the location of the corner diffractor, the scattered S-wave is used (Fig. 16a red box). The arrivals other than the scattered S waves are filtered and muted out. Fig. 16b shows the *f*–*k* filtered and muted shot gather obtained from the shot gather given in Fig. 16a. The remaining scattered S-wavefield (Fig. 16b) is used in the SI procedure described in Section 2.2. In Fig. 16c–e the retrieved ghost scattered S-waves for virtual-source locations at receivers 26, (29 m), 30

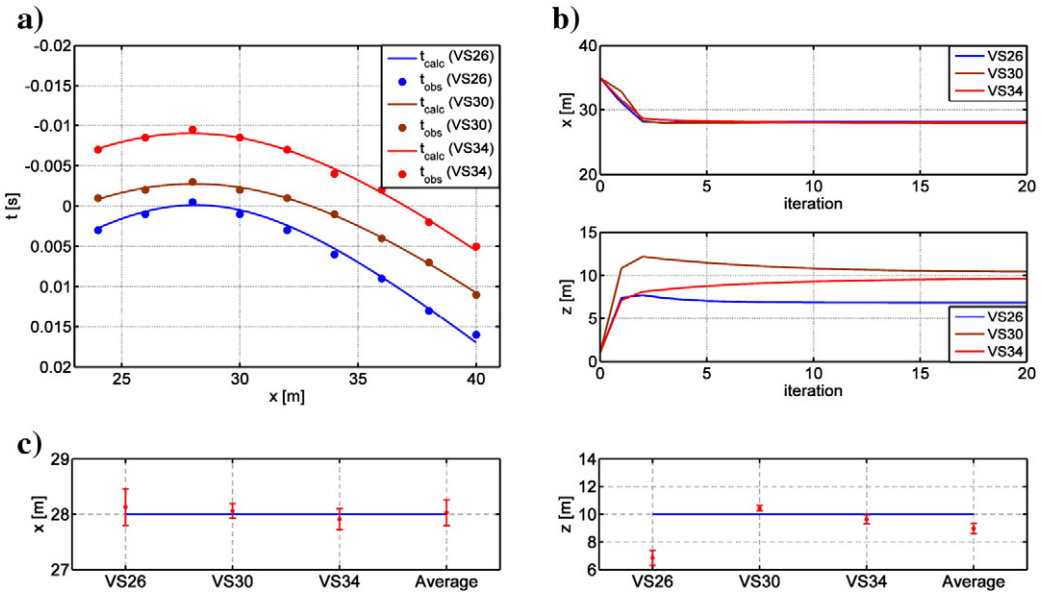

Fig. 17. (a) Observed (dots) and calculated (solid line) traveltimes; (b) estimated horizontal and vertical location of the corner diffractor for virtual sources 26 (blue, 29 m), 30 (brown, 33 m) and 34 (red, 37 m). The values at the zeroth iteration correspond to the initial parameters of the inversion. (c) Estimated model parameters and their 95% confidence limits, the blue line shows the location of the diffractor labeled A in Fig. 12. (For interpretation of the references to color in this figure legend, the reader is referred to the web version of this article.)

Table 6
The actual location (AL), the initial location (IL) for inversion and the estimated model parameters for different virtual source (VS) locations for the corner diffractor given in Fig. 12. E_t and E_m are the % errors of the traveltimes and model parameters calculated by Eqs. (8) and (9), respectively. σ_x and σ_z are standard deviations calculated from the diagonal of the model covariance matrix (Eq. (6)) and used in calculation of the 95% confidence levels (1.96 σ).

	AL (m)	IL (m)	VS 26 (m)	E_m (%)	VS 30 (m)	E_m (%)	VS 34 (m)	E_m (%)	Averaged (m)	E_m (%)
x	28.00	35.00	28.13	0.46	28.06	0.21	27.91	0.32	28.03	0.10
z	10.00	1.00	6.86	31.4	10.44	4.40	9.63	3.70	8.97	10.23
$\mp\sigma_X$			0.1680		0.0680		0.0964		0.1185	
$\mp\sigma_Z$			0.2760		0.1030		0.1617		0.1944	
E_t (%)			0.4404		0.1754		0.2830			

(33 m) and 34 (37 m) are given, respectively. To have a closer look at the retrieved scattered S-waves, the correlation results are plotted between −0.05 and 0.05 s. The selected ghost traveltime curves are shown in red in Fig. 16c–e.

The location of the corner diffractor is estimated again using the ghost traveltime relation Eq. (2) and SVD for inversion by Eq. (3). The best fit between the observed and calculated traveltimes of the ghost scattered S-waves for virtual sources 26, 30 and 34 (29, 33 and 37 m) are given in Fig. 17a and the initial (also given in Table 6) and the updated model parameters for each iteration are given in Fig. 17b. Fig. 17c shows the estimated model parameters and their 95% confidence intervals for each of the virtual-source location, while the last value is the average for the different virtual sources. The blue lines in Fig. 17c represent the location of the corner diffractor. It can be seen that the horizontal location is very well estimated. The 95% confidence interval includes the actual location of the scatterer. The average from the estimated values is x = 28.03 m whose error is 0.10%. The estimation of the depth for virtual-source location 26 is less accurate when compared to the virtual-source locations 30 and 34. Note that at the position of this virtual source the recorded scattered S-wave is much weaker compared to the arrivals at the other traces, which would lead to a relatively poorer correlation result. If we consider the estimation of the depth for virtual-source location 26 as an outlier, than the error in the estimated averaged depth will be about 0.4% instead of 10%.

4. Discussions

The results from the numerical models show the accuracies we can obtain in practice. The accuracies depend on how well we can isolate the scattered waves that we want to use for ghost retrieval. In the case of surface waves, if the direct waves can be adaptively subtracted, we obtain better estimation. But the interferometric adaptive surface-wave subtraction is an expensive operation. The cheaper *f–k* filtering is a less accurate operation and the result is larger individual errors in the estimated scatterer location.

In the numerical examples, the velocity is assumed to be a known parameter and we invert for the location of the scatterer and the corner diffractor. On the other hand, the body- and surface-wave velocities can also be considered as unknown and included in the inversion process; the initial velocities for the inversion can be estimated from the direct arrivals of the surface and body waves. Since the inverse problem is sensitive to the initial parameters, an additional unknown parameter may affect the stability of the inversion. Including the velocity as unknown parameter is planned for a future study.

In subsection 3.1.1, we suppressed the direct surface waves by interferometric prediction and subtraction. Note that the prediction process resulted not only in direct waves, but also in weak scattered surface waves (Fig. 8c). If a virtual source is created at a trace where the scattered surface-wave arrival has been strongly suppressed, the retrieved ghost scattered surface waves in this virtual-source gather would be of a poor quality. As a consequence, application of the inversion step to this gather might result in a poor estimation of the scatterer parameters. Such results should be treated as outliers.

In this study, we considered 2D models. For these situations, one could attempt estimating location of the scatterers using retrieved physical surface waves. For the 2D examples, retrieving physical scattered surface waves is possible as the active sources are along the stationary-phase line that connects the receivers and the scatterers. Note that for 3D problems, locating an offline scatterer may become quite difficult when attempting to use retrieved physical arrivals from it. To retrieve physical scattered waves in 3D, multiple sources would be required at least in a patch (e.g. Halliday et al., 2010), but in the general case a closed boundary of active sources would be required. To understand the effects of a 3D medium in estimating the location of the scatterer using our method, both 3D numerical modelling and an ultrasonic laboratory experiment are planned. We expect that, using our method as few as three active sources perpendicular to the line of the receivers would suffice.

In the examples in the previous section, we estimated approximately the midpoint of the scatterer, for which we observed the highest amplitude of the correlated traces. If the size of the scatterer is sufficiently large to allow observation of the scattering from its corner, then the estimation of the size of the scatterer would be possible. Otherwise, the estimations will be within the uncertainty limits.

In the models in this paper, we considered single isolated scatterers. In case of multiple scatterers, the estimation of the locations could be possible, if the scattered wavefields of each scatterer can be observed separately or separated from each other (for example using muting). This can be related to the physical properties, sizes and the distances between the scatterers. If the scatterers are close to one another in a wavelength sense, their scattered wavefields will constructively or destructively interfere and the recorded resulting scattered wavefield will be a combination of the two. In such cases, we would be able to estimate the parameters of the "combined" scatterer.

Although the examples were for the geotechnical scale, the proposed method is not restricted to geotechnical studies only. It can also be used in exploration and global seismology for detecting and characterizing scatterers. For example for the larger scale, locating a buried fault could be possible with our technique.

5. Conclusions

We proposed a method for estimating the location of a near-surface scatterer or diffractor by using traveltimes of non-physical (ghost) scattered surface and body waves obtained by from seismic interferometry. The ghost scattered waves are obtained by cross-correlating the recorded scattered waves originating from only one source at the surface. The traveltimes of the ghost scattered waves are used in an inversion to find the location of the scatterer and a corner diffractor. The depth and the horizontal position of the objects are obtained for different virtual-source locations.

An advantage of our proposed method is that the unwanted travel paths between the source and the receiver array are eliminated. These travel paths can traverse a complicated medium. Due to the elimination of these paths, the calculation times for waveform inversion can be reasonably reduced. Also when lateral changes of the medium properties are present, these path effects are eliminated by interferometry and locations closer to the target are considered for estimation of the location of the scatterer.

We tested our method on four numerically modelled datasets with increasing complexity. We demonstrated that the location of the scatterer can be estimated from ghost scattered waves with a good accuracy. We also showed that the quality of the estimated locations of the objects depend on the quality of the estimated scattered wavefields.

Acknowledgments

This work is supported by TUBITAK (The Scientific and Technological Research Council of Turkey) with the project 110Y250 titled "Detecting Near-surface Scatterers by Inverse Scattering and Seismic Interferometry of Scattered Surface Waves" and by Istanbul Technical University Research Fund with the project "Estimating the Location of the Scatterers by Seismic Interferometry". We gratefully acknowledge these financial supports. The investigations of D.D. were supported by the Division for Earth and Life Sciences (ALW) with financial aid from the Netherlands Organization for Scientific Research (NWO). We also thank the Colorado School of Mines for providing the Seismic Un*x (Cohen and Stockwell, 2012) package as open source software.

References

Al-fares, W., Bakalowicz, M., Guérin, R., Dukhan, M., 2002. Analysis of the karst aquifer structure of the Lamalou area (Hérault, France) with ground penetrating radar. Journal of Applied Geophysics 51, 97–106.

Bodet, L., Galibert, P.Y., Dhemaied, A., Camerlynck, C., Al-Zoubi, A., 2010. Surface-wave Profiling for Sinkhole Hazard Assessment Along the Eastern Dead Sea Shoreline, Ghor Al-Haditha, Jordan. Extended Abstracts of the 72st EAGE Meeting, Barcelona, p. M027.

Boiero, B., Socco, L.V., 2010. Retrieving lateral variations from surface wave dispersion curves. Geophysical Prospecting 1–20.

Bozdag, E., Kocaoglu, A.H., 2005. Estimation of site amplifications from shear-wave velocity profiles in Yesilyurt and Avcilar, Istanbul, by frequency-wavenumber analysis of microtremors. Journal of Seismology 9 (1), 87–98.

Campman, X., Riyanti, C.D., 2007. Non-linear inversion of scattered seismic surface waves. Geophysical Journal International 171, 1118–1125.

Campman, X., van Wijk, K., Riyanti, C.D., Scales, J., Herman, G., 2004. Imaging scattered seismic surface waves. Near Surface Geophysics 2 (4), 223–230.

Canıtez, N., Toksöz, M.N., 1971. Focal mechanism and source depth of earthquakes from body- and surface-wave data. Bulletin of the Seismological Society of America 61, 1369–1379.

Cardarelli, E., Cercato, M., Cerreto, A., Di Filippo, G., 2010. Electrical resistivity and seismic refraction tomography to detect buried cavities. Geophysical Prospecting 58 (4), 685–695.

Chai, H.Y., Phoon, K.K., Goh, S.H., Wei, C.F., 2012. Some theoretical and numerical observations on scattering of Rayleigh waves in media containing shallow rectangular cavities. Journal of Applied Geophysics 83, 107–119.

Chang, S., Baag, C., 2005. Crustal structure in Southern Korea from joint analysis of teleseismic receiver functions and surface-wave dispersion. Bulletin of the Seismological Society of America 95, 1516-1234.

Cohen, J.K., Stockwell Jr., J.W., 2012. CWP/SU: Seismic Un*x Release No. 43: An Open Source Software Package for Seismic Research and Processing. Center for Wave Phenomena, Colorado School of Mines.

Cong, L., Mitchell, B.J., 1998. Seismic velocity and Q structure of the Middle Eastern crust and upper mantle from surface-wave dispersion and attenuation. Pure and Applied Geophysics 153, 503–538.

Culshaw, M.G., Waltham, A.C., 1987. Natural and artificial cavities as ground engineering hazards. The Quarterly Journal of Engineering Geology 20, 139–150.

Debeglia, N., Bitri, A., Thierry, P., 2006. Karst investigations using microgravity and MASW: application to Orleans, France. Near Surface Geophysics 4, 215–225.

Dong, S., He, R., Schuster, G.T., 2006. Interferometric Prediction and Least-squares Subtraction of Surface Waves. 76th Annual International Meeting, SEG, Expanded Abstracts, pp. 2783–2786.

Draganov, D., Wapenaar, K., Mulder, W., Singer, J., Verdel, A., 2007. Retrieval of reflections from seismic background-noise measurements. Geophysical Research Letters 34, L04305.

Draganov, D., Campman, X., Thorbecke, J., Verdel, A., Wapenaar, K., 2009. Reflection images from ambient seismic noise. Geophysics 74 (5), A63–A67.

Draganov, D., Heller, K., Ghose, R., 2012. Monitoring CO_2 storage using ghost reflections retrieved from seismic interferometry. International Journal of Greenhouse Gas Control 11S, S35–S46.

Edmonds, C.N., 2008. Karst and mining geohazards with particular reference to the Chalk outcrop, England. Quarterly Journal of Engineering Geology & Hydrogeology 41, 261–278.

Ekström, G., 2006. Global detection and location of seismic sources by using surface waves. Bulletin of the Seismological Society of America 96 (4A), 1201–1212.

Engelsfeld, T., Šumanovac, F., Pavin, N., 2008. Investigation of underground cavities in a two-layer model using the refraction seismic method. Near Surface Geophysics 6 (4), 221–231.

Engelsfeld, T., Šumanovac, F., Krstić, V., 2011. Classification of near-surface anomalies in the seismic refraction method according to the shape of the time–distance graph: a theoretical approach. Journal of Applied Geophysics 74 (1), 59–68.

Foti, S., 2000. Multistation Methods for Geotechnical Characterization using Rayleigh Waves. Ph.D. dissertation, Ingegneria Geotecnica, Universuty deli Studi.

Gelis, C., Leparoux, D., Virieux, J., Bitri, A., Operto, S., Grandjean, G., 2005. Numerical modeling of surface waves over shallow cavities. Journal of Environmental and Engineering Geophysics 10 (2), 111–121.

Grandjean, G., Leparoux, D., 2004. The potential of seismic methods for detecting cavities and buried objects: experimentation at a test site. Journal of Applied Geophysics 56 (2), 93–106.

Halliday, D.F., Curtis, A., 2008. Seismic surface waves in a suburban environment: active and passive interferometric methods. The Leading Edge 27 (2), 210–218.

Halliday, D.F., Curtis, A., 2009. Seismic interferometry of scattered surface waves in attenuative media. Geophysical Journal International 185, 419–446.

Halliday, D.F., Curtis, A., Robertsson, J.O.A., van Manen, D.J., 2007. Interferometric surface-wave isolation and removal. Geophysics 72 (5), A69–A73.

Halliday, D.F., Curtis, A., Vermeer, P., Strobbia, C., Glushchenko, A., van Manen, D.J., Robertsson, J.O.A., 2010. Interferometric ground-roll removal: attenuation of scattered surface waves in single-sensor data. Geophysics 75 (2), A15–A25.

Harmankaya, U., Kaslilar, A., Thorbecke, J., Wapenaar, K., Draganov, D., 2012a. Estimating the Location of Scatterers by Seismic Interferometry of Scattered Surface Waves. Extended Abstracts of the 74st EAGE Meeting, Copenhagen, p. X008.

Harmankaya, U., Kaslilar, A., Thorbecke, J., Wapenaar, K., Draganov, D., 2012b. Estimation of the Location of a Scatterer from Interferometric Ghosts of the Scattered Surface Waves. Extended Abstracts of the Istanbul International Geophysical Conference and Oil & Gas Exhibition, Istanbul, p. 173.

Herman, G.C., Milligan, P.A., Huggins, R.J., Rector, J.W., 2000. Imaging shallow objects and heterogeneities with scattered guided waves. Geophysics 65 (1), 247–252.

Kaslilar, A., 2007. Inverse scattering of surface waves: imaging of near-surface heterogeneities. Geophysical Journal International 171, 352–367.

Khomenko, V.P., 2008. Forecast of a collapse location: new approach. Quarterly Journal of Engineering Geology & Hydrogeology 41, 393–401.

Kimman, W.P., Trampert, J., 2010. Approximations in seismic interferometry and their effects on surface waves. Geophysical Journal International 182, 461–476.

King, S., Curtis, A., 2012. Suppressing nonphysical reflections in Green's function estimates using source-receiver interferometry. Geophysics 77, Q15–Q25.

Kocaoglu, A.H., Fırtana, K., 2011. Estimation of shear wave velocity profiles by the inversion of spatial autocorrelation coefficients. Journal of Seismology 15 (4), 613–624.

Kovach, R.L., 1978. Seismic surface waves and crustal and upper mantle structure. Review of Geophysics and Space Physics 16, 1–13.

Leparoux, D., Bitri, A., Grandjean, G., 2000. Underground cavity detection: a new method based on seismic Rayleigh waves. EJEEG 5, 33–53.

McCann, D.M., Jackson, P.D., Culshaw, M.G., 1987. The use of geophysical surveying methods in the detection of natural cavities and mineshafts. The Quarterly Journal of Engineering Geology 20, 59–73.

Mikesell, T.D., van Wijk, K., Blum, T.E., 2012. Analyzing the coda from correlating scattered surface waves. Journal of the Acoustic Society of America 131 (3), EL275–EL281.

Mohanty, P.R., 2011. Numerical modeling of P-waves for shallow subsurface cavities associated with old abandoned coal workings. Journal of Environmental and Engineering Geophysics 16 (4), 165–175.

Nasseri-Moghaddam, A., Cascante, G., Jean Hutchinson, J., 2005. A new quantitative procedure to determine the location and embedment depth of a void using surface waves. Journal of Environmental and Engineering Geophysics 10 (1), 51–64.

Nazarian, S., Stokoe, K.H., Hudson, W.R., 1983. Use of spectral analysis of surface waves method for determination of moduli and thicknesses of pavement systems. Transportation Research Record 930, 38–45.

Nuzzo, L., Leucci, G., Negri, S., 2007. GPR, VES and refraction seismic surveys in the karstic area "Spedicaturo" near Nociglia (Lecce, Italy). Near Surface Geophysics 5 (1), 67–76.

O'Neill, A., 2003. Full waveform reflectivity for modeling, inversion and appraisal of seismic surface wave dispersion in shallow site investigations. Ph.D. dissertation, University of Western Australia, Perth.

Park, C.B., Miller, R.D., Xia, J., 1999. Multichannel analysis of surface waves. Geophysics 64 (3), 800–808.

Randall, M.R., Zandt, G., 2007. Inverse Problems in Geophysics, Lecture Notes, Dept. of Geosciences, University of Arizona, Tucson, Arizona 8521.

Rix, G.J., Hebeler, G.L., Orozco, M.C., 1998. Near-surface Vs profiling in the New Madrid seismic zone using surface wave methods. Seismological Research Letters 73 (3), 380–392.

Rodríguez-Castellanos, A., Sánchez-Sesma, F.J., Luzón, F., Martin, R., 2006. Multiple scattering of elastic waves by subsurface fractures and cavities. Bulletin of the Seismological Society of America 96 (4A), 1359–1374.

Roux, P., Sabra, K.G., Gerstoft, P., Kuperman, W.A., Fehler, M.C., 2005. P-waves from cross-correlation of seismic noise. Geophysical Research Letters 32, L193031–L193034.

Ruigrok, E., Campman, X., Draganov, D., Wapenaar, K., 2010. High-resolution lithospheric imaging with seismic interferometry. Geophysical Journal International 183, 339–357.

Samyn, K., Bitri, A., Grandjean, G., 2012. Imaging a near-surface feature using cross-correlation analysis of multi-channel surface wave data. Near Surface Geophysics 10. http://dx.doi.org/10.3997/1873-0604.2012007.

Schuster, G.T., 2009. Seismic Interferometry. Cambridge University Press, Cambridge.

Schuster, G.T., Yu, J., Sheng, J., Rickett, J., 2004. Interferometric/daylight seismic imaging. Geophysical Journal Internatinal 157, 838–852.
Sens-Schönfelder, C., Wegler, U., 2006. Passive image interferometry and seasonal variations of seismic velocities at Merapi volcano, Indonesia. Geophysical Research Letters 33, L21302.
Shapiro, N.M., Campillo, M., 2004. Emergence of broadband Rayleigh waves from correlations of the ambient seismic noise. Geophysical Research Letters 31, L07614.
Snieder, R., 1987. Surface wave holography. In: Nolet, G. (Ed.), Seismic tomography. D. Reidel Publishing, Dordrecht, pp. 323–337.
Snieder, R., 2004. Extracting the Green's function from the correlation of coda waves: a derivation based on stationary phase. Physical Review E 69, 046610.
Snieder, R., Wapenaar, K., 2010. Imaging with ambient noise. Physics Today 63 (9), 44–49.
Snieder, R., Wapenaar, K., Larner, K., 2006. Spurious multiples in seismic interferometry of primaries. Geophysics 71, SI111–SI124.
Socco, L.V., Boiero, D., 2008. Improved Monte Carlo inversion of surface wave data. Geophysical Prospecting 56, 357–371.
Socco, L.V., Boiero, D., Wisén, R., Foti, S., 2009. Laterally constrained inversion of ground roll of seismic reflection records. Geophysics 74 (6), G35–G45.
Socco, L.V., Jongmans, D., Boiero, D., Stocco, S., Tokeshi, K., Maraschini, M., Hantz, D., 2010. Geophysical investigation of the Sandalp rock avalanche deposits. Journal of Applied Geophysics 70 (4), 277–291.
Thorbecke, J., Draganov, D., 2011. Finite-difference modeling experiments for seismic interferometry. Geophysics 75, H1–H18. http://dx.doi.org/10.1190/GEO2010-0039.1.
van Manen, D., Curtis, A., Robertsson, J.O.A., 2006. Interferometric modeling of wave propagation in inhomogeneous elastic media using time reversal and reciprocity. Geophysics 71 (4), SI47–SI60.
Wapenaar, K., 2004. Retrieving the elastodynamic Green's function of an arbitrary inhomogeneous medium by cross correlation. Physical Review Letters 93 (25), 254301.
Wapenaar, K., Fokkema, J., 2006. Green's function representations for seismic interferometry. Geophysics 71 (4), SI33–SI46.
Woodcock, N.H., Omma, J.E., Dickson, J.A.D., 2006. Chaotic breccia along the Dent Fault, NW England: implosion or collapse of a fault void? Journal of the Geological Society 163, 431–446.
Xia, J., Nyquist, J.E., Xu, Y.X., Roth, M.J.S., Miller, R.D., 2007. Feasibility of detecting near-surface feature with Rayleigh-wave diffraction. Journal of Applied Geophysics 62 (3), 244–253.
Xia, J., Xu, Y., Miller, R.D., Zeng, C., 2010. A trade-off solution between model resolution and covariance in surface-wave inversion. Pure and Applied Geophysics 167 (12), 1537–1547.
Xu, C., Butt, S.D., 2006. Evaluation of MASW techniques to image steeply dipping cavities in laterally inhomogeneous terrain. Journal of Applied Geophysics 59 (2), 106–116.